

Computational Study of the Allosteric Effects of p5 on CDK5–p25 Hyperactivity as Alternative Inhibitory Mechanisms in Neurodegeneration

Tejaswi Tammareddy, Walid Keyrouz, Ram D. Sriram, Harish C. Pant, Antonio Cardone,* and Jeffery B. Klauda*



Cite This: <https://doi.org/10.1021/acs.jpcc.2c02868>



Read Online

ACCESS |



Metrics & More

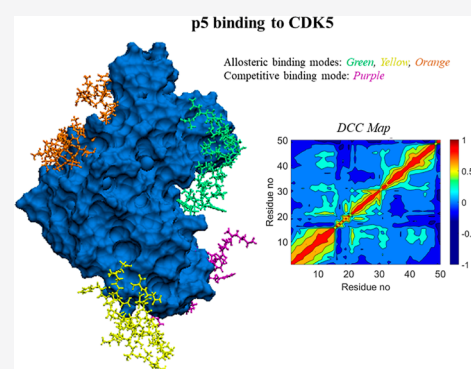


Article Recommendations



Supporting Information

ABSTRACT: The cyclin-dependent kinase (CDK5) forms a stable complex with its activator p25, leading to the hyperphosphorylation of tau proteins and to the formation of plaques and tangles that are considered to be one of the typical causes of Alzheimer's disease (AD). Hence, the pathological CDK5–p25 complex is a promising therapeutic target for AD. Small peptides, obtained from the truncation of CDK5 physiological activator p35, have shown promise in inhibiting the pathological complex effectively while also crossing the blood–brain barrier. One such small 24-residue peptide, p5, has shown selective inhibition toward the pathological complex *in vivo*. Our previous research focused on the characterization of a computationally predicted CDK5–p5 binding mode and of its pharmacophore, which was consistent with competitive inhibition. In continuation of our previous work, herein, we investigate four additional binding modes to explore other possible mechanisms of interaction between CDK5 and p5. The quantitative description of the pharmacophore is consistent with both competitive and allosteric p5-induced inhibition mechanisms of CDK5–p25 pathology. The gained insights can direct further *in vivo/in vitro* tests and help design small peptides, linear or cyclic, or peptidomimetic compounds as adjuvants of orthosteric inhibitors or as part of a cocktail of drugs with enhanced effectiveness and lower side effects.



1. INTRODUCTION

The protein cyclin-dependent kinase (CDK5) is an atypical member of the CDK family implicated in the regulation of many neuronal functions, including learning and memory, through the phosphorylation of several cytoskeletal proteins.¹ Under physiological conditions, CDK5 function requires binding with activators such as p35 or p39.² In the event of oxidative stress with Ca²⁺ influx, the protease calpain is activated and it cleaves the p35 into two fragments: p25 and p10.^{3,4} The p25 protein thus formed can bind to CDK5, deregulating its activity and leading to hyperphosphorylation of tau proteins. This results in the formation of β -amyloid plaques, neurofibrillary tangles and senile plaques, hallmarks of neurodegenerative diseases such as Alzheimer's disease (AD), Parkinson's disease, and amyotrophic lateral sclerosis (ALS).^{5,6} Thus, the CDK5–p25 complex has emerged as a therapeutic target for AD and other neurodegenerative diseases.⁷

Earlier research on the inhibition of CDK5–p25 activity involved drugs targeting the adenosine 5'-triphosphate (ATP) binding pocket of CDK5 (phosphorylation is required for the activation of CDK5 to carry out its endogenous function), such as aminothiazole and roscovitine.^{8,9} However, due to the lack of selective inhibition of the CDK5–p25 pathological complex, these drugs resulted in reduced efficacy and side effects. There are other types of drugs under research such as antioxidants and

those targeting the clearance of plaques,¹⁰ whose efficacy and safety need further investigation.^{11,12} Common drugs in current use, such as acetylcholinesterase inhibitors¹³ and NMDA receptor antagonists,¹⁴ can slow down the progression of the disease but do not stop it or reverse it. The use of small peptides obtained from truncating p35 has proven, experimentally, to selectively inhibit the pathological activity caused by the CDK5–p25 complex without affecting the physiological function of CDK5–p35.¹⁵ The peptide p5 is one such peptide known to selectively inhibit CDK5–p5 pathology without affecting CDK5–p35 physiology both *in vivo* and *in vitro*,^{16,17} and can be tagged to promote crossing of the blood–brain barrier¹⁸ making it a promising lead drug candidate. However, a structure-based approach for developing viable candidates has been hampered by our limited knowledge of the binding mechanisms of p5 to CDK5.

Received: April 25, 2022

Revised: June 14, 2022

We previously computationally predicted¹⁹ five CDK5–p5 binding modes using a method based on configurational biased Monte Carlo (MC) sampling. We focused on a specific stable binding mode, involving the CDK5–p25 binding pocket and hence consistent with competitive inhibition of the pathological complex. The analysis enabled us to derive a pharmacophore from the main stabilizing interactions of the CDK5–p5 complex. We found electrostatic and H-bond interactions to be dominant in stabilizing the binding between p5 and CDK5 consistently across four of the six replicates.

In this paper, we comprehensively study the mechanism of inhibition of p5 by analyzing four additional binding modes outside the CDK5–p25 binding pocket that might lead to allosteric effects. Three critical structural elements representing important functional regions of CDK5 are targeted in our analysis (Figure 1): the ATP binding pocket, with a fundamental

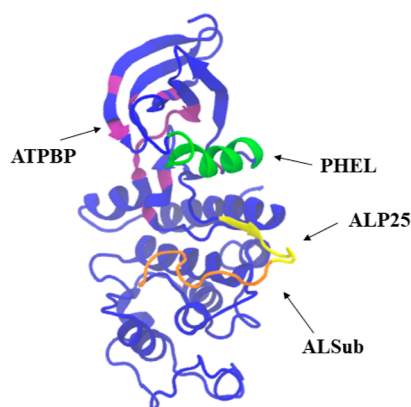


Figure 1. Important structural elements of CDK5: PSAALRE helix (PHEL) in green, activation loop on p25 binding side (ALP25) in yellow, activation loop on substrate binding side (ALSub) in orange, and ATP binding pocket (ATPBP) in purple.

role in the phosphorylation of substrates, resulting from CDK5 activation;²⁰ the activation loop, separated into p25-binding and substrate-binding parts; the PSAALRE helix, that is known to form a wedge-shaped cavity along with the activation loop to accommodate the activators.^{21,22} Henceforth, these structural elements are referred to as PHEL (PSAALRE helix), ATPBP (ATP binding pocket), ALP25 (p25 binding side of the activation loop), and ALSub (substrate binding side of the activation loop).

The four binding modes we predicted previously¹⁹ and investigated here are shown in Figure 2. In modes *c1* and *c3*, the p5 binding occurs at the CDK5 mainly on the N-terminal domain (NTD or small lobe), in the vicinity of the ATPBP without occluding ATP access, with p5 taking helix-turn-helix form. In mode *c2*, the p5 binding occurs at the C-terminal domain (CTD or large lobe), with p5 adopting a disordered conformation. In mode *c4*, the p5 binding occurs in proximity of the p25 binding side of the activation loop with p5 in a single helix form. Our analysis of these modes provides a complete picture of all the p5-induced inhibition mechanisms, both orthosteric and allosteric, that can be exploited to reverse the deregulated hyperactivity. Furthermore, the derivation of the corresponding pharmacophores may help guide QSAR experiments for designing drug-like compounds against AD.

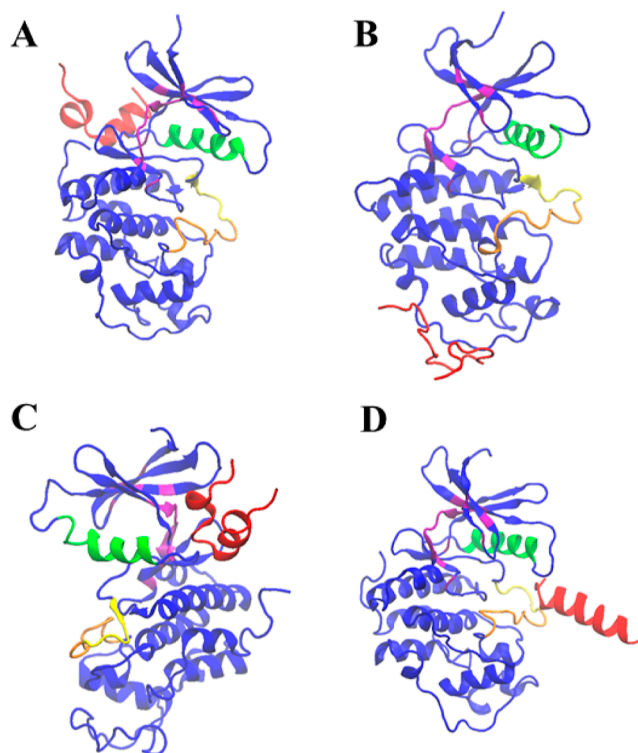


Figure 2. CDK5–p5 binding modes *c1* (A), *c2* (B), *c3* (C), and *c4* (D). The kinase CDK5 in blue, the peptide p5 in red, the ATP binding pocket (ATPBP) in purple, the PSAALRE helix (PHEL) in green, the p25 binding portion of the activation loop (ALP25) in yellow, and the substrate binding portion of the activation loop (ALSub) in orange are shown for each mode.

2. METHODS

2.1. CDK5–p5 Binding Mode Prediction. The method employed to predict CDK5–p5 binding modes is similar to our previous work¹⁹ and is summarized here. The CDK5 structure that was used represents a large conformational family that was identified using molecular dynamics (MD) simulations.¹⁹ Such conformational family notably includes the CDK5 active state from the crystal structure of the CDK5–p25 complex (PDB ID: 1UNL).^{23,24} On the other hand, the p5 structures were obtained based on the 24-amino acid sequence ¹KEAFWDRCLS-VINLMSSKMLQINA²⁴ from the literature.²⁵ We used a stochastic conformational optimization method based on MC minimization/annealing (MCMA),²⁶ followed by replica exchange Langevin dynamics simulations. For both the steps, we employed the standard all-atom CHARMM36(C36) force field^{27–29} and the SCP implicit solvent model.^{30,31} The resulting ensemble of p5 structures was clustered into four large conformational families.¹⁹

Starting from the above CDK5 and p5 conformations, we predicted CDK5–p5 binding using a method that involves two main steps.³² First, a prescreening of favorable binding modes was carried out using simulated annealing MC simulations based on coarse-grained electrostatic and hydrophobic interaction norms.¹⁹ Subsequently, adaptive biased MC simulations were performed using the all-atom CHARMM36(C36) force field^{27–29} and the SCP implicit solvent model.^{30,31} The configurational biasing function was defined based on the ensemble of prescreened binding modes previously identified.¹⁹ The five binding modes thus identified were finally refined using MD simulations as described below.

2.2. System Setup and MD Simulations Protocol. The CHARMM-GUI Solvator^{27,33,34} was used for each of the above CDK5–p5 binding modes to obtain the input files for the MD simulations carried out in this work. Systems were built in a tetragonal box with explicit water solvent. The CHARMM36-(C36)-compatible TIP3P water model was used.^{29,35,36} Counterions of K⁺ and Cl[−] amounting to 0.1 M concentration were added to neutralize the system. Simulations were performed at a body temperature of 310.15 K and at 1 atm pressure. Initially, a 10,000 step *NVT* (constant particle number, volume, and temperature ensemble) minimization was performed³⁷ to eliminate bad steric contacts. Subsequently, the system was equilibrated for 0.07 ns. Finally, 500 ns (except system *c3*) production runs were performed using *NPT* (constant particle number, isotropic pressure, and temperature ensemble) simulations.³⁸ In the case of binding mode *c3*, only 100 ns production runs were performed due to the instability of the binding mode and henceforth the mode is discarded from the analysis. The temperature was held constant by Langevin dynamics³⁹ and the pressure is kept constant by the Nosé–Hoover–Langevin piston.^{22,38,40} The particle mesh Ewald method was used for full-system periodic electrostatics with an interpolation order of 6 and grid spacing of 1 Å.^{41–43} A force-based switching function was used for van der Waals with a cutoff of 12 Å.⁴² The simulations were performed using NAMD,⁴⁴ and three replicates were obtained for each binding mode. Henceforth, the three replicates for a given binding mode *cx* are called *cx_r1*, *cx_r2*, *cx_r3*, with *x* = 1, 2, 3, 4. The simulations were carried out on four GPU compute nodes of the MARCC cluster, consisting of 14-core processors and 2 NVIDIA K80 GPUs per node. The average performance was ~23.8 ns/day for the system consisting of ~72,000 atoms with one compute node. Trajectory analysis was performed on a single node with six cores in the *express* partition of MARCC clusters.

2.3. Trajectory Analysis Methods. We compared the molecular trajectories of stable CDK5–p5 binding modes with the unbound CDK5 to reveal the effect of p5 binding on CDK5 dynamic behavior. The comparison was carried out focusing on the relevant structural elements of CDK5 discussed earlier.

We employed three complementary approaches to characterize the effect of p5 binding on CDK5, which are described below. It is important to observe that the focus is on CDK5 internal dynamics changes induced by p5 binding. Hence, the frames of each trajectory are preliminarily aligned based on the *C_α* of CDK5 and without including atoms of the CDK5 structural element of interest (*ALP25*, *ALSub*, *PHEL*, and *ATPBP*) to eliminate the effect of rigid motions on the analysis and to focus on the dynamics of interest. The alignment and the subsequent computation of principal component analysis (PCA) and dynamic cross correlation (DCC) maps are performed using the Bio3D package in R.^{45,46}

2.3.1. PCA-Based Analysis. The PCA-based approach relies on the covariance matrix built from the molecular trajectory. The covariance matrix of coordinate deviations reflects the correlation between atomic motions, and it is defined as⁴⁷

$$\mathbf{Cov} = \langle (\mathbf{x} - \langle \mathbf{x} \rangle)(\mathbf{x} - \langle \mathbf{x} \rangle)^T \rangle \quad (1)$$

where \mathbf{x} is a 3N-dimensional vector of coordinates, *N* is the number of atoms considered, and $\langle \rangle$ denotes a time average. Upon diagonalization of the covariance matrix **Cov**, a set of 3N eigenvalues and corresponding eigenvectors is obtained, representing collective motions of the protein. Each eigenvalue

is a measure of the magnitude of the corresponding collective motion, and the projection of the corresponding eigenvector onto a given atom is a measure of the magnitude of the motion of such atom. Large eigenvalues and the corresponding eigenvectors represent the most significant degrees of freedom of the dynamics, and they likely capture important positional fluctuations. These include mutually perpendicular displacements, unlike the cross-correlation matrix discussed below. This analysis provides insights into collective motions induced within CDK5 in any possible direction as a result of binding with p5. Herein, we accounted for at least 80% (of eigenvalues) of the overall random motions observed in the protein throughout the simulation in each trajectory.

PCA analysis enables the comparison of collective motions across different trajectories focusing on the above-defined structural elements *ALP25*, *ALSub*, *PHEL*, and *ATPBP*. This can be done by projecting each eigenvector onto the atoms belonging to a structural element of interest and by weighing the resulting average projection using the corresponding eigenvalue. This can be formally defined as

$$\mathbf{CMM}_{\text{str},i} = EV_i \times \|\vec{e}_i\|_{\text{str}} \quad (2)$$

where $\mathbf{CMM}_{\text{str},i}$ represents a measure of the magnitude of the collective motion for a structural element *str* based on the *i*th eigenvalue. In eq 2, EV_i is the magnitude of the *i*th eigenvalue and $\|\vec{e}_i\|_{\text{str}}$ is the average magnitude of the projection of the *i*th eigenvector onto the atoms belonging to the structural element *str*.

2.3.2. DCC-Based Analysis. The correlation matrix,⁴⁸ unlike the covariance matrix discussed above, specifically targets atom movements in the same (correlated) or opposite (anti-correlated) direction. Therefore, correlation analysis is less general than PCA, but it ensures that strongly correlated or anti-correlated dynamic motions, possibly missed in the PCA approach, are detected. Formally, the *i*–*j*th entry of the correlation matrix is defined as

$$C_{ij} = \frac{\langle \Delta r_i \times \Delta r_j \rangle}{\langle \Delta r_i^2 \rangle^{1/2} \langle \Delta r_j^2 \rangle^{1/2}} \quad (3)$$

where $\langle \rangle$ denotes a time average and Δr_i is the displacement of atom *i* between two consecutive trajectory frames. The correlation matrix values defined in eq 3 are between 1 (perfect correlation occurring, by definition, at the matrix principal diagonal) and −1 (perfect anti-correlation).

2.3.3. Root Mean Square Fluctuation-Based Analysis. Additional evidence of the effect of p5 binding on CDK5 was obtained from the molecular trajectories by computing the average root mean square fluctuation (RMSF) of the atomic positions. The RMSF quantifies the average deviation of an atom, or a group of atoms, from a reference position over time. Generally, the reference represents a time-averaged position. Hence, in this case, all CDK5 frames are aligned to the reference position before the RMSF calculation. This leads to the identification of the structural elements with the largest fluctuations with respect to their average position. RMSF-based analysis can help identify additional significant fluctuations about an average position, induced in CDK5, that are neither correlated nor collective motions, obtained by DCC maps and PCA-based analysis, respectively.

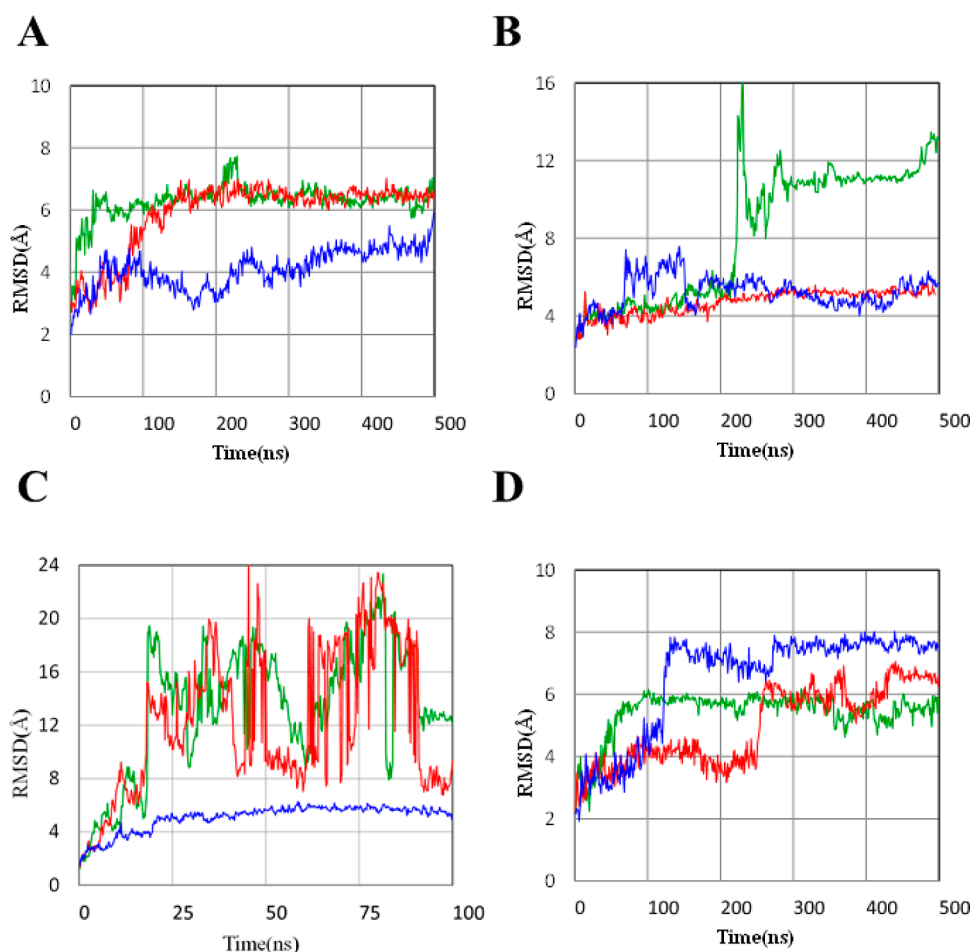


Figure 3. CDK5-based RMSD, computed on the p5 backbone after aligning the CDK5 backbone, is shown for the binding modes *c1*, *c2*, *c3*, and *c4* represented by (A–D), respectively. The three replicates *r1*, *r2*, and *r3* are represented in red, green, and blue, respectively, for each binding mode. Please note that the *c3* system was simulated for 100 ns only (see text). Refer to Figures S1–S5 for further insights into some of the events resulting in the dynamic shifts observed here.

3. RESULTS

In order to investigate the inhibition mechanisms of peptide p5, MD simulations were performed. For each stable binding mode, we investigated changes in the dynamics of each CDK5 structural element (Figure 1) upon binding with the peptide p5. Such changes were evaluated by quantitatively comparing them to the unbound CDK5. The four binding modes (Figure 2) were subjected to MD simulations in three replicates, as discussed in Section 2. In the following section, we present our findings from the root mean square deviation (RMSD)-based analysis as well as from the trajectory analysis approaches discussed earlier. The respective pharmacophores provide quantitative insights into the molecular features of interest.

3.1. p5 Binding Stability and Conformational Analysis.

Initially, we computed the RMSD for each replicate of the four binding modes to verify the stability of CDK5–p5 binding. The RMSD is a standard measure of structural distance between arbitrarily selected groups of atoms. Here, the focus is the stability of p5 with respect to its initial binding with CDK5. However, it is reasonable to expect that p5 will also go through significant conformational changes throughout the simulation.

In order to study both CDK5–p5 binding stability and the occurrence of p5 conformational changes, two RMSD computations were carried out. First, the trajectory frames were aligned to the first frame based on the CDK5 backbone,

and the RMSD was subsequently computed on p5 backbone atoms (CDK5-based RMSD). Second, the trajectory frames were aligned to the first frame based on the p5 backbone, and the RMSD was subsequently computed on p5 backbone atoms (p5-based RMSD). The p5-based RMSD accounts for p5 conformational changes, whereas the CDK5-based RMSD mainly accounts for the stability of p5 with respect to its initial binding with CDK5. However, the outcome of the CDK5-based RMSD computation can be also affected by p5 conformational changes, especially if they are significant. Therefore, only the combined analysis of the two RMSD computations, along with visual inspection of the trajectories (Figures S1–S5), yields an insightful interpretation of the data. Furthermore, in order to get additional insights into the conformational changes in p5, in some cases we evaluated the secondary structure as a function of time.

The CDK5-based (Figure 3) and p5-based (Figure 4) RMSD are shown for the three replicates of modes *c1*, *c2*, *c3*, and *c4*. For mode *c1*, the CDK5-based RMSD reaches a plateau for all replicates after an initial sharp increase, suggesting an initial binding switch followed by binding stability. Visual inspection suggests that the binding pocket for all replicates is almost coincident after a slight translation from the initial binding site. As far as p5 conformational changes, in all replicates of mode *c1* the peptide p5 retains a helical structure at the C-terminus,

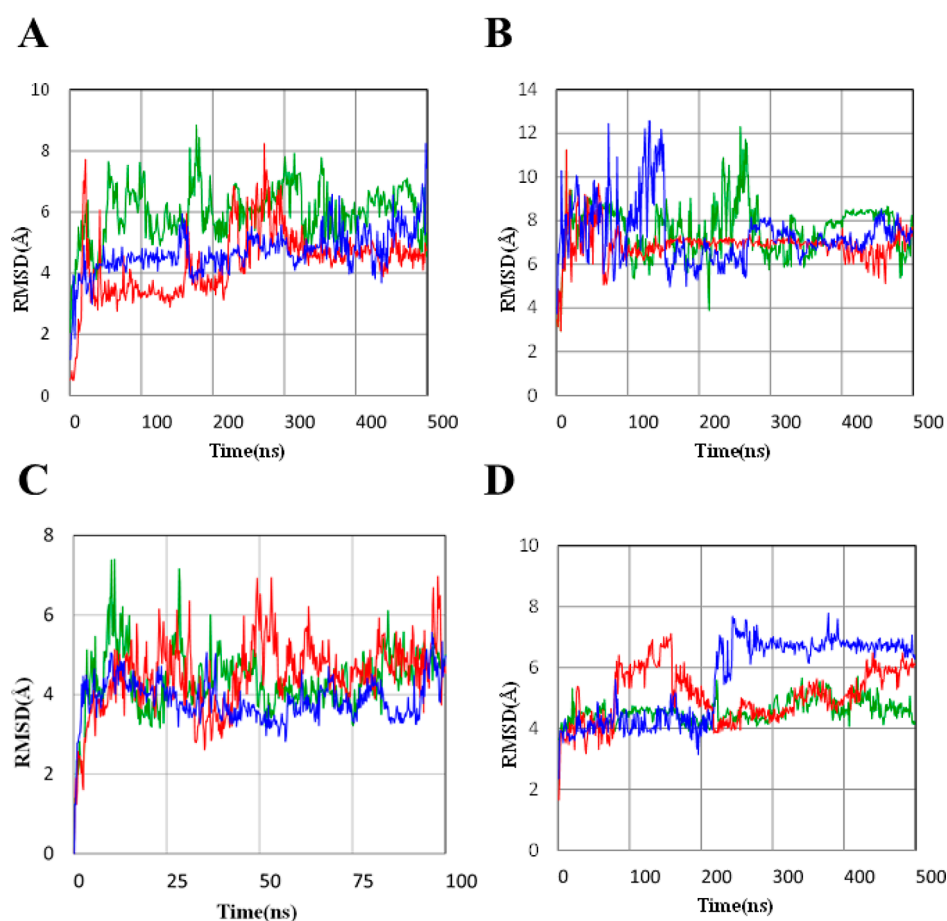


Figure 4. p5-based RMSD, which is calculated on the p5 backbone after aligning its backbone, is shown for the binding modes *c1*, *c2*, *c3*, and *c4* represented by (A–D), respectively. The three replicates *r1*, *r2*, and *r3* are represented in red, green, and blue, respectively for each binding mode. Please note that the *c3* system was simulated for 100 ns only (see text).

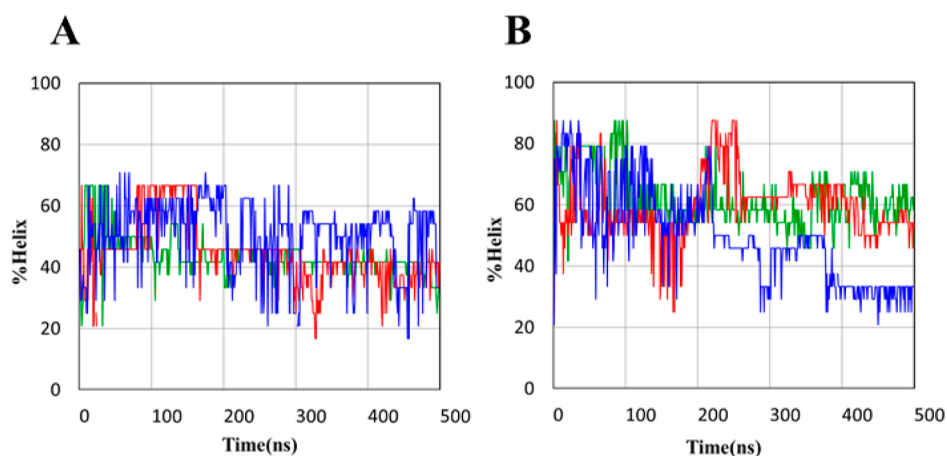


Figure 5. Secondary structure of p5 as a function of time for the binding modes *c1* (A) and *c4* (B). The replicates *r1*, *r2*, and *r3* are represented in red, green, and blue, respectively.

which is stable, and a coiled structure at the N-terminus. The plot of p5 secondary structure as a function of time (Figure 5A) shows a 5–10% decrease in the percentage of helical structure of p5 for replicates *c1_r1* and *c1_r2*, whereas for *c1_r3* it remains almost constant throughout the simulation. These changes in secondary structure are consistent with the increase in the p5-based RMSD for these replicates. Therefore, it is reasonable to infer that the high values of the CDK5-based RMSD for

replicates *c1_r1* and *c1_r2* result from an initial shift in binding, whereas the peaks in the p5-based RMSD result from the loss of α -helical secondary structure. The secondary structure of each residue of peptide p5 as a function of time is presented for all replicates of *c1* in Figure S6.

For mode *c2*, a sudden increase in the CDK5-based RMSD is visible for the replicate *c2_r2*. That, in combination with data from the p5-based RMSD and visual inspection, suggests that

Table 1. Binding Stability, Main Binding Features, and Potential Inhibition Type for Each Mode/Replicate

| mode | binding stability | stable binding location(s) | potential inhibition type (based on CDK5–p25 binding pocket) |
|--|---------------------------|--|--|
| <i>c1_r1</i> | stable after early switch | close to the ATP binding pocket (<i>ATPBP</i>) | non-competitive |
| <i>c1_r2</i> | stable after early switch | close to the ATP binding pocket (<i>ATPBP</i>) | non-competitive |
| <i>c1_r3</i> | stable | close to the ATP binding pocket (<i>ATPBP</i>) | non-competitive |
| <i>c2_r1</i> | stable | close to the helix-dominant region of CDK5 (large lobe) | non-competitive |
| <i>c2_r2</i> | unstable | | |
| <i>c2_r3</i> | stable | close to the helix-dominant region of CDK5 (large lobe) | non-competitive |
| <i>c3_r1</i> | unstable | | |
| <i>c3_r2</i> | unstable | | |
| <i>c3_r3</i> | stable | between the ATP binding pocket (<i>ATPBP</i>) and the PSAALRE helix (<i>PHEL</i>) | non-competitive |
| <i>c4_r1_a</i> (initial 250 ns of <i>c4_r1</i>) | stable | close to the PSAALRE helix (<i>PHEL</i>) and activation loop (<i>ALP25</i> and <i>ALSub</i>) | competitive |
| <i>c4_r1_b</i> (final 250 ns of <i>c4_r1</i>) | stable | close to the activation loop (<i>ALP25</i> and <i>ALSub</i>) | non-competitive |
| <i>c4_r2</i> | stable | close to the PSAALRE helix (<i>PHEL</i>) and activation loop (<i>ALP25</i> and <i>ALSub</i>) | competitive |
| <i>c4_r3</i> | stable after early switch | close to the activation loop (<i>ALP25</i> and <i>ALSub</i>) | competitive |

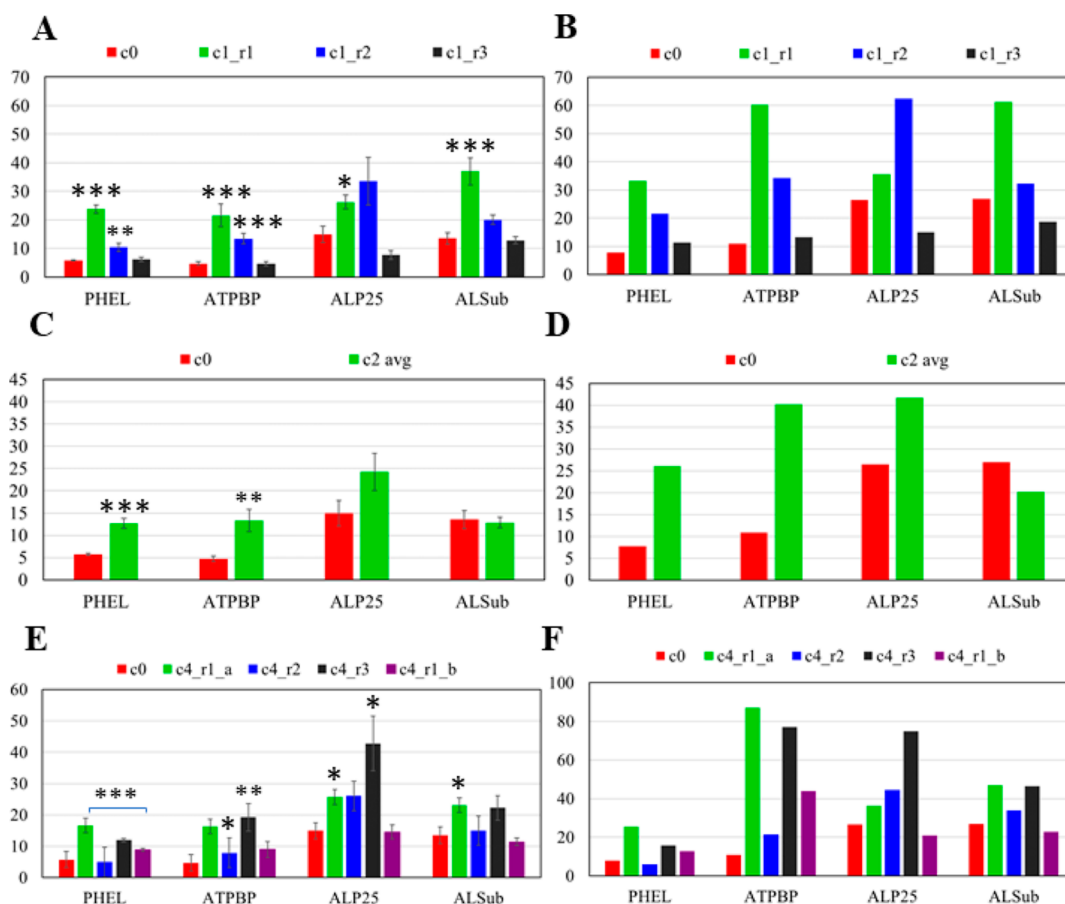


Figure 6. Average (left) and maximum (right) values of the collective structural motions (eq 2) over the three large eigenvalues for modes *c1* (A,B), *c2* (C,D), and *c4* (E,F) replicates and the control *c0* (* represents $p < 0.05$, ** represents $p < 0.005$, *** represents $p < 0.0005$). In *c2*, eigenvalues for the two analyzed replicates (average value) are presented. The data are organized based on CDK5 structural elements and the bars are color coded based on simulation replicates. The control system is represented in red and *cx_r1*, *cx_r2*, and *cx_r3* are represented in green, blue, and black, respectively. For replicate *c4_r1*, the data are presented separately for the initial (*c4_r1_a*) and final part (*c4_r1_b*) of the trajectory in green and purple, respectively (please refer to text).

the CDK5–p5 binding does not hold. Therefore, we only analyze replicates *c2_r1* and *c2_r3*, whose binding remains stable throughout the simulation. As far as p5 conformational

changes, the complete lack of p5 secondary structure leads to large fluctuations of the C-terminus that are evident from the RMSD data and visual inspection, especially for replicate *c2_r3*.

Although there is no secondary structure in $c2_r3$ at the beginning of the simulation, at around 200 ns there is a B-sheet formation observed. The secondary structure changes are presented in Figure S7 for $c2_r1$ and $c2_r3$ as a function of simulation time for each residue in p5.

For mode $c3$, a sudden increase in the CDK5-based RMSD is visible for two replicates. Evidence from the p5-based RMSD and visual inspection as well confirm that p5 detaches from CDK5 in those replicates. Therefore, mode $c3$ is discarded altogether in our analysis.

For mode $c4$, sudden increases in the CDK5-based RMSD are visible for all replicates. The initial binding pocket involves the CDK5 activation loop and the PSAALRE helix, both belonging to the CDK5 binding site with the pathological activator p25. For replicate $c4_r1$, a binding switch occurs at about half of the trajectory. The new binding site is located at CDK5 large lobe, and it involves CDK5 activation loop. For replicates $c4_r2$ and $c4_r3$, there is also a switch in the CDK5–p5 binding pocket, this time early on (at approximately 250 ns for the former and 120 ns for the latter). The binding switch consists of a pivoting motion of p5 around its N-terminus, which remains stably bound to CDK5. In both cases, the pivoting motion results into a stable binding still involving the CDK5 binding site with the pathological activator p25. As far as p5 conformational changes, replicate $c4_r2$ remains generally stable but the peptide loses around 20% of its helical structure (Figure 5B) by the end of the simulation. On the other hand, for replicate $c4_r1$ the coiled C-terminus pivots throughout the trajectory, and it eventually retracts into a bent conformation. In $c4_r3$, there is a gradual and significant reduction (around 50%, refer to Figure 5) in the helical structure of the peptide by the end of the trajectory. This probably also contributes to the high p5-based RMSD values in Figure 4. A detailed representation of secondary structure of each residue in peptide p5 as a function of simulation time is presented for $c4$ in Figure S8 for further reference.

The initial and stabilized binding sites are shown for each replicate that was selected for analysis in Figures S1–S5. In Table 1, the findings discussed above are summarized. The competitive or non-competitive nature of the inhibition potentially associated with each binding mode is also reported, based on the involvement of the CDK5–p25 binding pocket. As discussed above, CDK5–p5 binding does not remain stable for $c2_r2$ and for two replicates of mode $c3$, which is discarded from further analysis. All CDK5–p5 bindings in mode $c4$ involve the CDK5–p25 binding pocket, hence they are potentially consistent with competitive inhibition. Finally, for replicate $c4_r1$ because the pre- and post-binding shift portions of the trajectories are stable and of comparable length, they are analyzed separately.

3.2. PCA-Based Dynamics Analysis. The dynamic behavior of CDK5 in the unbound state and upon binding with p5 in modes $c1$, $c2$, and $c4$ was compared based on the covariance matrix computed on the trajectories as described in Section 2 (eqs 1 and 2). In Figure 6, the average collective structural motions (eq 2) over the three largest eigenvalues are shown for the three above-listed binding modes and for the control simulation $c0$ (unbound CDK5). The maximum collective structural motions are also shown to gain additional insights. The data are reported separately for each CDK5 structural element of interest. Apart from the important structural elements, a detailed residue-by-residue analysis of the contribution to the overall collective motions is presented

for each binding mode in comparison with the control system (unbound CDK5) in Figure S9.

For mode $c1$, the p5 binding with CDK5 occurs in proximity of ATPBP for all replicates (Table 1). The data shows statistically significant changes in the average collective ATPBP motion with respect to the control simulation $c0$ in two out of three replicates, possibly due to the proximity of the CDK5–p5 binding pocket (Figure 6A). Allosteric effects on ALP25, ALSUB, and PHEL are also present, as statistically significant differences of the related average collective motions with respect to the control $c0$ are evident in Figure 6A. The maximum collective structural motions for all CDK5 structural elements increase in replicates $c1_r1$ and $c1_r2$. On the other hand, for binding mode $c1_r3$ the maximum collective ALP25 and ALSUB motion decrease (Figure 6B).

For mode $c2$, the binding of p5 with CDK5 occurs at the bottom of the large lobe, away from all structural elements (Table 1). Statistically significant differences in the average collective structural motions with respect to the control $c0$ involve both PHEL and ATPBP (Figure 6C), suggesting the presence of allosteric effects. For mode $c2$, the two analyzed replicates behave similarly and therefore the data are averaged. An overall increase in the maximum values of the collective structural motions is shown in Figure 6D for all CDK5 structural elements except ALSUB.

The binding mode $c4$ initially involves the structural elements ALP25 and PHEL, both belonging to the CDK5–p25 binding pocket. Therefore, the mode represents a possible instance of competitive inhibition. For replicate $c4_r1$, the initial binding is stable and occurs mainly nearby PHEL. Subsequently, there is a shift in the binding site of p5 at 250 ns, after which the binding switches more toward ALP25 (Table 1). Therefore, the PCA data in Figure 6E are presented separately for the initial ($c4_r1_a$) and final ($c4_r1_b$) parts of the trajectory in this replicate. Statistically significant changes with respect to the control occur in the average collective motions of PHEL, ATPBP, and ALP25 for replicate $c4_r1_a$, indicating both allosteric and non-allosteric effects (Figure 6E). For replicate $c4_r1_b$, statistically significant changes of the collective motions with respect to the control only take place for PHEL, representing allosteric effects in this case. For replicates $c4_r2$ and $c4_r3$, p5-triggered changes in the collective motions can be observed on PHEL and ATPBP, where the latter represents an allosteric effect. Both $c4_r1_a$ and $c4_r3$ show a clear increase in the maximum values of the collective structural motions (Figure 6F).

3.3. DCC-Based Dynamics Analysis. The correlated dynamics of structural elements in the unbound CDK5 and in the CDK5–p5 binding modes $c1$, $c2$, and $c4$ were compared based on the DCC computed on the trajectories as described in Section 2 (Equation 3). The DCC was computed separately for each CDK5 structural element pair based on the C_α . Before performing DCC analysis, we aligned the protein based on the atoms C_α not belonging to the structural elements of interest. In Figure 7, the average DCC is shown for each structural element pair. The corresponding correlation data are presented in Table S1. The data are presented for all analyzed replicates of the binding modes $c1$, $c2$, and $c4$ as well as for the control simulation $c0$. The non-averaged DCC maps obtained for each residue of all the important structural elements are presented in Figure S10 for further reference.

For all replicates of mode $c1$, most structural elements show significant changes in their correlated motions with respect to

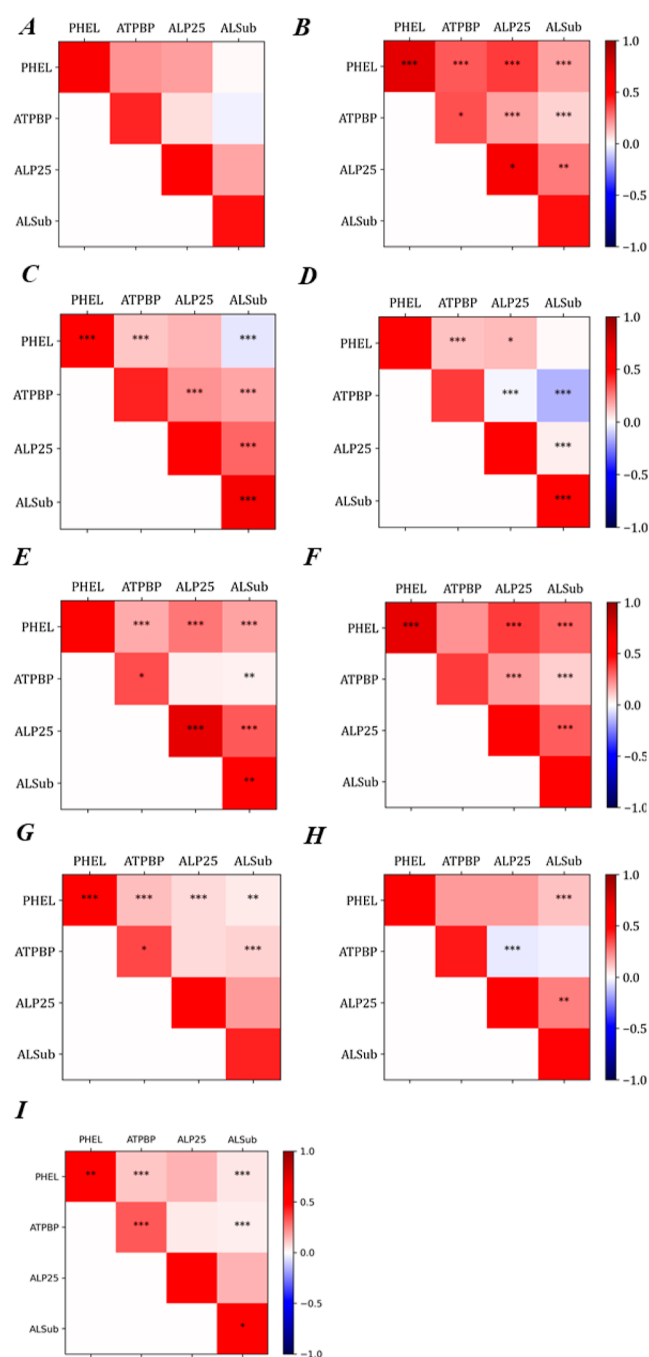


Figure 7. DCC maps for $c1_r1$, $c1_r2$, $c1_r3$, $c2$, $c4_r1_a$, $c4_r2$, $c4_r3$, and $c4_r1_b$ represented by (B–I), respectively, in comparison with the control $c0$ (A). In mode $c2$, DCC maps are presented for a representative replicate. For replicate $c4_r1$, the data are presented separately for the initial ($c4_r1_a$) and final part ($c4_r1_b$) of the trajectory [(F,I), respectively, please refer to text]. (* represents $p < 0.05$, ** represents $p < 0.005$, *** represents $p < 0.0005$).

the control simulation $c0$ (Figure 7). In particular, as evident from Figure 7, there is a switch from correlated (in the control) to anti-correlated movement between *ALSub* and *PHEL* in replicate $c1_r2$ and between *ATPBP* and *ALSub* in replicate $c4_r3$.

For mode $c2$, all replicates behave similarly and therefore the data are shown for a representative replicate. Once again, most structural elements show significant changes in correlation with respect to the control simulation $c0$. Among these, the correlated

motions of higher significance are those of *PHEL* with *ATPBP*, *ALP25*, and *ALSub*.

For replicates $c4_r1_a$ and $c4_r1_b$ of mode $c4$, representing the initial and final portion of the replicate $c4_r1$, different correlated behaviors are observed, probably due to the shift in the binding site. In mode $c4_r2$, the positive correlation of *ATPBP* with *ALP25* and *ALSub* increases. On the other hand, there is an increase in the anti-correlated movement between *PHEL* and *ALSub*. Finally, replicate $c4_r3$ shows increased correlation between *ALSub* and *PHEL* and decreased anti-correlation between *ALP25* and *ATPBP* with respect to the control.

3.4. RMSF-Based Dynamics Analysis. The fluctuations of structural elements in the control (unbound CDK5) and in the CDK5–p5 binding modes $c1$, $c2$, and $c4$ were compared based on the RMSF, computed after aligning the backbone of CDK5 without including the structural elements of interest for the analysis. In Figure 8, the average and maximum RMSF is shown for each structural element, for the analyzed replicates of the binding modes $c1$, $c2$, and $c4$, and for the control simulation $c0$. A detailed all-residue RMSF for each binding mode is presented in comparison with the control $c0$ in Figure S11 for further reference.

In binding mode $c1$, the average RMSF of *ALSub* of $c1_r3$ is statistically different from the control. Furthermore, there is a considerable increase in the maximum RMSF of *ATPBP* for mode $c1_r1$, of *ALP25* for mode $c1_r2$, and of *ATPBP* and *ALSub* for mode $c1_r3$. In binding mode $c2$, there are statistically significant differences in the average RMSF of *PHEL* in both $c2_r1$ and $c2_r3$ and of *ALSub* in $c2_r3$. There is an increase in the maximum RMSF as well in both replicates for the structural elements *PHEL* and *ATPBP* and a decrease in replicate $c2_r3$ for *ALSub*. For binding mode $c4$, both $c4_r1_a$ and $c4_r1_b$ show statistically significant differences in the average RMSF of *ALSub*. On the other hand, in replicate $c4_r1_a$ there is a large increase in the maximum RMSF of *ATPBP*.

3.5. Contact Map-Based Analysis and Pharmacophores. In this section, we analyze the CDK5–p5 interactions for each binding mode and identify the specific amino acids involved as well as the nature of such interactions. The contact maps for each of the analyzed modes are shown in Figures S12–S14, at 100 ns intervals, for insights into the contact stability. Overall, for modes $c1$ and $c2$ and for replicate $c4_r2$ the contacts are stable throughout the trajectory, whereas for replicate $c4_r1$ the contacts are stable before and after the binding pocket switch. For replicate $c4_r3$, the binding is stable after an initial switch in the binding site. Henceforth, when a pair of amino acids is listed the first amino acid belongs to p5 and the second to CDK5. In Table 2, the most persistent amino acid interactions throughout the trajectories are listed for each mode. For each binding mode, the distance between these amino acids (i.e., specific atoms within them) is shown as a function of time in Figures S15–S18.

In binding mode $c1$ (Figure 9A), the peptide binds nearby the *ATPBP* and remains stable after an initial shift in the binding pocket. Herein, persistent amino acid interactions consist of hydrophobic contacts such as $I12_{p5}$ – $I135_{CDK5}$ and $L20_{p5}$ – $Y90_{CDK5}$. These interactions stabilize within 100 ns and remain consistent for the next 400 ns of the simulation (the resulting pharmacophore is shown in Figure 9A). Other contacts involve polar backbone (hydrogen bond) interactions between residue pairs $L20_{p5}$ – $P291_{CDK5}$ and $I12_{p5}$ – $K112_{CDK5}$. The residue pair $M19_{p5}$ – $N137_{CDK5}$ forms a hydrogen bond interaction between

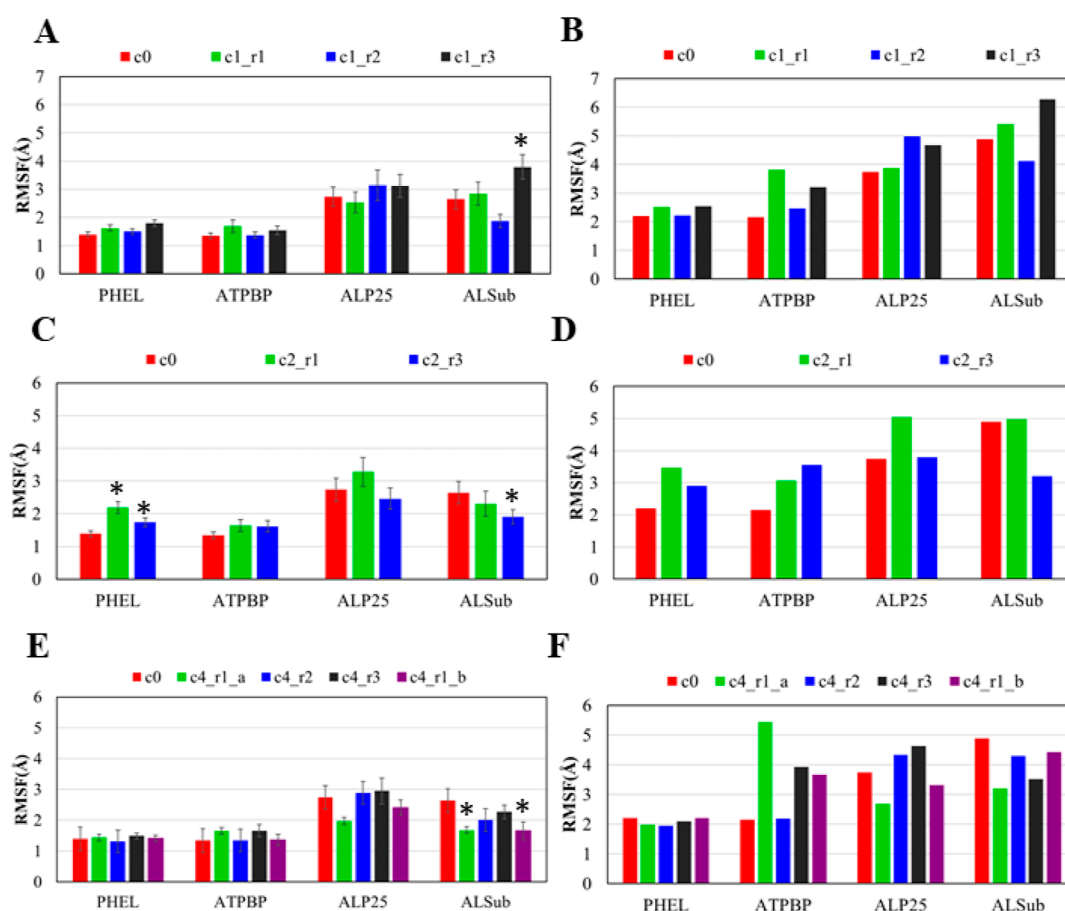


Figure 8. Average (top) and maximum (bottom) values of the RMSF for modes $c1$, $c2$, and $c4$ binding modes and the control $c0$ (* represents $p < 0.05$). The data are organized based on CDK5 structural elements and the bars are color coded based on simulation replicates. For replicate $c4_r1$, the data are presented separately for the initial and final part of the trajectory (please refer to text).

Table 2. Pharmacophores and the Predominant Nature of Binding Site Interactions for Each Binding Mode

| binding mode | $C1$ | $C2$ | $C4$ (competitive) | $C4_r1_b$ (non-competitive) |
|------------------------|---|--|--|---|
| pharmacophores | L20 _{p5} -P291 _{CDK5} I12 _{p5} -I134 _{CDK5} M19 _{p5} -N37 _{CDK5} L20 _{p5} -Y90 _{CDK5} I12 _{p5} -K112 _{CDK5} | W5 _{p5} -Y242 _{CDK5} W5 _{p5} -V251 _{CDK5} W5 _{p5} -L202 _{CDK5} F4 _{p5} -L218 _{CDK5} W5 _{p5} -F203 _{CDK5} | E2 _{p5} -R125 _{CDK5} F4 _{p5} -L147 _{CDK5} V11 _{p5} -Y15 _{CDK5} E2 _{p5} -R194 _{CDK5} E2 _{p5} -R195 _{CDK5} | A24 _{p5} -S180 _{CDK5} A24 _{p5} -T181 _{CDK5} N23 _{p5} -L178 _{CDK5} Q21 _{p5} -L178 _{CDK5} I22 _{p5} -P271 _{CDK5} |
| nature of interactions | hydrophobic and polar backbone | hydrophobic | hydrophobic and salt bridges | Hydrophobic and polar backbone |

the sulfur atom of methionine and the side chain nitrogen atom of asparagine, which becomes stable from 100 ns onward.

In binding mode $c2$ (Figure 9B), the predominant interaction is a hydrophobic core between CDK5 and p5, involving the peptide N-terminus. For binding mode $c4$, competitive and non-competitive interactions are evaluated separately and two different pharmacophores are evaluated. For the competitive interactions, salt bridges between glutamic acid and arginine are predominant in three out of the five stable interacting residue pairs that were identified. The other stable residue pairs form a hydrophobic core region between CDK5 and p5. Herein this binding mode, the N-terminus of p5 binds close to PHEL, ALP25, and ALSub (Figure 9C). After the switch to a competitive binding site, the C-terminus of the peptide binds away from PHEL and close to ALP25 and ALSub (Figure 9D). In the competitive binding mode $c4_r1_b$, the predominant nature of the interactions for the stable residue pairs is also

hydrophobic. For the residue pair I22_{p5}-P271_{CDK5}, a polar backbone interaction can be observed after stabilization, which occurs in the first 100 ns.

4. SUMMARY AND DISCUSSION

Herein, we predicted binding modes using the previously developed MCMA method based on coarse-grained electrostatic and hydrophobic interactions followed by biased sampling in implicit solvent (refer to Section 2). Most of the binding modes remained stable throughout the 500 ns simulation. Only $c3$ and $c2_r2$ were found to be unstable and hence discarded from further analysis. In replicate $c4_r1$, we analyzed two separate trajectories of 250 ns each to account for a significant switch in the binding site. An early shift in the binding site was also observed in modes $c1$ and $c4$, occurring within the first 100–200 ns of the simulation (Figures S1–S5). In all cases, the post-switch binding remained stable and hence the trajectory was

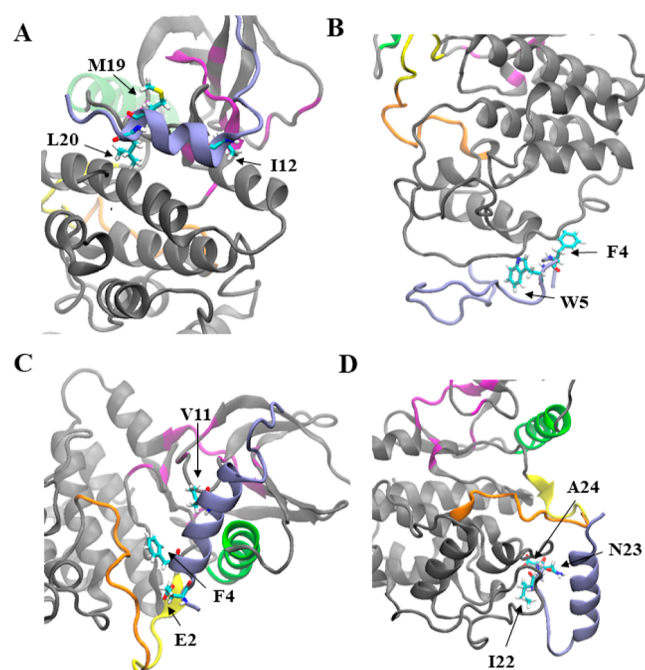


Figure 9. Snapshots of CDK5–p5 binding modes. Persistently interacting residues of the peptide p5 are explicitly indicated for each binding mode. The peptide p5 is represented in blue, the activation loop in yellow (ALP25) and orange (ALSub), the ATP binding pocket (ATPBP) in purple, and the PSAALRE helix (PHEL) in green. Binding modes *c1*, *c2*, and *c4* are represented in panels (A–C), respectively. Panel (D) represents the non-competitive replicate *c4_r1_b* (please refer to text).

considered for further analysis. The binding shifts that occurred in some of the simulations could be the result of sampling inaccuracies associated to the binding prediction method, and in particular associated to the coarse-grained models used in the first step. We also characterized conformational changes of the peptide, with focus on its secondary structure. We found that mode *c2* assumes a coiled form lacking helical structure without significantly changing its binding with CDK5. On the other hand, in modes *c1* and *c4* we identified a reduction in the percentage of the peptide helical structure (Figure 5) as time progressed. These secondary structure changes could have influenced the shift in the binding site from the predicted one. Arguably, such binding shifts might be the result of artifacts in the binding prediction method because it allows no or limited protein flexibility in the early binding stages.²⁶ Insights from this work can be used to enhance the binding prediction method, for instance by taking into account non-rigid interactions early on and hence more closely mimicking secondary structure shifts and other important structural changes.

We investigated the stable binding modes to identify any statistically significant difference in collective or correlated motions that were induced in CDK5 as a result of binding with p5. This was achieved using three computational tools: DCC maps, PCA, and RMSF. The DCC maps indicate p5-induced changes in correlated motions involving important structural elements for most of the binding modes when compared with the control system (unbound CDK5). All these changes involve structural elements that are not in close proximity to the binding pockets, suggesting the presence of allosteric effects. DCC maps also suggest the presence of allosteric effects in all binding modes except for *c4_r1_a*.

In addition, we used PCA to study collective motions, not necessarily correlated, to complement the insights from DCC maps. Akin DCC maps, PCA led to the identification of significant p5-induced dynamic motions in most of the binding modes, the majority of which are consistent with allosteric effects. For example, in *c1_r1* we identify collective motions, not present in the control system, involving all structural elements although the binding occurs close to ATPBP. This is clear evidence of the presence of allosteric effects. A summary of these findings is presented in Table S2. The system *c4_r1_a* involves no allosteric effects based on both PCA and DCC maps but is consistent with competitive inhibition. The only system with inconsistent data between PCA and DCC is *c1_r3*, in which the allosteric effects observed from the DCC analysis are not present based on the PCA analysis. This mode is also not consistent with competitive inhibition. The inconsistency might be due to the presence of correlated motions that are not detected in PCA analysis. Ultimately, based on DCC and PCA analyses, all the replicates except for *c1_r3* and *c4_r1_a* show the allosteric effect.

We also analyzed the binding modes by computing the RMSF, which characterizes the fluctuations of all the residues about an average position. Based on the RMSF, we identified allosteric effects in *c1_r3*, *c2_r1* and *c2_r3* (Table S2).

Finally, contact maps were evaluated to characterize the binding sites and the predominant nature of the interactions. We identified a completely different interaction pattern in comparison with the previously identified pharmacophore (Cardone et al. 2016¹⁹), which mostly involves electrostatic interactions. Instead, the binding modes discovered here mostly involve hydrophobic interactions, with only few instances of backbone hydrogen bonding interactions. Furthermore, the interactions associated to the competitive mode *c4* are different from the previously identified and also competitive K1-E2-E24_{p5} pharmacophore.¹⁹

The above summarized work led to the discovery of potential novel mechanisms of inhibition of the pathological CDK5–p25 complex by peptide p5, in addition to the competitive inhibition mechanism discovered in our previous work. One important observation is that, in this work, the use of three different complementary approaches enabled the investigation of all possible modes of inhibition of CDK5–p25 with p5. This was of key importance for the discovery of novel p5-induced inhibition mechanisms, many of which represent allosteric effects.

The novel pharmacophores identified here are significantly different from the previous study and warrant further investigation. To this end, we believe that the identification and characterization of the specific amino acid pairs involved in each inhibitory mode will enable targeted mutagenesis studies whereby systematically mutating the residues of p5 in vitro and in vivo, based on the data presented in Table 2, would enable the validation of our findings. More specifically, combinatorial mutations with adverse and non-adverse, single and double mutations would enable probing such mechanisms.

Please note that the identified pharmacophores are closer to the C- and N-termini, which were not capped in our simulations. This should be considered in the setup of the experimental mutagenesis studies. Furthermore, among the three stable binding modes investigated, *c2* is the only one without helical secondary structure for p5 (disordered structure). This results in potentially increased flexibility of p5 and it likely allows more p5 residues to be available for binding with CDK5. Therefore, mutagenesis studies might be less insightful for this mode

because mutations might inadvertently trigger artificial binding mechanisms due to p5 flexibility. On the other hand, modes *c1* and *c4* show a mainly helical secondary structure for p5, which likely keeps the peptide more stable and better amenable to controlled mutagenesis studies. It is unclear which form of p5 would be a better template for a drug candidate, but a more rigid structure might be more amendable to a highly specific target as compared to one with disorder.

Overall, the work presented here shows evidence for formerly unknown, potential allosteric effects induced in CDK5 as a result of its binding with p5. Thorough trajectory analysis led to the discovery of novel pharmacophores involving amino acids close to the termini of the peptide p5, mainly associated with hydrophobic interactions. This work, in combination with our previous¹⁹ study, offers a potential route to design enhanced peptides, derived from p5, that can more efficiently inhibit the pathological CDK5–p25 complex.

■ ASSOCIATED CONTENT

SI Supporting Information

The Supporting Information is available free of charge at <https://pubs.acs.org/doi/10.1021/acs.jpbc.2c02868>.

DCC values for each replicate, systematic sorting of the binding mechanism based on the data and the binding site location, binding site shift and lack thereof, real-time secondary structure information for each residue in p5, dynamics data for all the residues in CDK5, and contact maps at regular intervals of simulation time and interacting atom/residue distances as a function of time for all the interacting residue pairs (PDF)

■ AUTHOR INFORMATION

Corresponding Authors

Antonio Cardone – Information Systems Group, National Institute of Standards and Technology, Gaithersburg, Maryland 20899, United States; Email: antonio.cardone@nist.gov

Jeffery B. Klauda – Department of Chemical and Biomolecular Engineering and Institute for Physical Science & Technology, Biophysics Graduate Program, University of Maryland, College Park, Maryland 20742, United States; orcid.org/0000-0001-8725-1870; Email: jbklauda@umd.edu

Authors

Tejaswi Tammareddy – Department of Chemical and Biomolecular Engineering, University of Maryland, College Park, Maryland 20742, United States; Information Systems Group, National Institute of Standards and Technology, Gaithersburg, Maryland 20899, United States

Walid Keyrouz – Information Systems Group, National Institute of Standards and Technology, Gaithersburg, Maryland 20899, United States

Ram D. Sriram – Software and Systems Division, Information Technology Laboratory, National Institute of Standards and Technology, Gaithersburg, Maryland 20899, United States

Harish C. Pant – Neuronal Cytoskeletal Protein Regulation Section, Laboratory of Neurochemistry, NINDS, Bethesda, Maryland 20892, United States

Complete contact information is available at: <https://pubs.acs.org/doi/10.1021/acs.jpbc.2c02868>

Notes

The authors declare no competing financial interest.

Disclaimer: Commercial products are identified in this document in order to specify the experimental procedure adequately. Such identification is not intended to imply recommendation or endorsement by the National Institute of Standards and Technology nor is it intended to imply that the products identified are necessarily the best available for the purpose.

■ ACKNOWLEDGMENTS

This work was supported by the National Institute of Standards and Technology (NIST) through the Professional Research Experience Program (PREP). Dr. Sergio A. Hassan (National Institute of Allergy and Infectious Diseases) contributed to the implementation of the molecular docking software and to the subsequent prediction of the CDK5–p5 binding modes studied in this paper. High-performance clusters provided by the Maryland Advanced Research Computing Center (MARCC) and NIST were used in this research. The University of Maryland HPC cluster, Deepthought2, was used for trajectory analysis.

■ REFERENCES

- (1) Tan, T. C.; Valova, V. A.; Malladi, C. S.; Graham, M. E.; Berven, L. A.; Jupp, O. J.; Hansra, G.; McClure, S. J.; Sarcevic, B.; Boadle, R. A.; Larsen, M. R.; Cousin, M. A.; Robinson, P. J. Cdk5 is essential for synaptic vesicle endocytosis. *Nat. Cell Biol.* **2003**, *5*, 701–710.
- (2) Dhavan, R.; Tsai, L.-H. A decade of CDK5. *Nat. Rev. Mol. Cell Biol.* **2001**, *2*, 749–759.
- (3) Lee, M.-s.; Kwon, Y. T.; Li, M.; Peng, J.; Friedlander, R. M.; Tsai, L.-H. Neurotoxicity induces cleavage of p35 to p25 by calpain. *Nature* **2000**, *405*, 360–364.
- (4) Lapresa, R.; Agulla, J.; Sánchez-Morán, I.; Zamarrño, R.; Prieto, E.; Bolaños, J. P.; Almeida, A. Amyloid- β promotes neurotoxicity by Cdk5-induced p53 stabilization. *Neuropharmacology* **2019**, *146*, 19–27.
- (5) Monaco, E. A., 3rd Recent evidence regarding a role for Cdk5 dysregulation in Alzheimer's disease. *Curr. Alzheimer Res.* **2004**, *1*, 33–38.
- (6) Maccioni, R. B.; Muñoz, J. P.; Barbeito, L. The molecular bases of Alzheimer's disease and other neurodegenerative disorders. *Arch. Med. Res.* **2001**, *32*, 367–381.
- (7) Allnut, A. B.; Waters, A. K.; Kesari, S.; Yenugonda, V. M. Physiological and Pathological Roles of Cdk5: Potential Directions for Therapeutic Targeting in Neurodegenerative Disease. *ACS Chem. Neurosci.* **2020**, *11*, 1218–1230.
- (8) Shah, R. S.; Lee, H.-G.; Xiongwei, Z.; Perry, G.; Smith, M. A.; Castellani, R. J. Current approaches in the treatment of Alzheimer's disease. *Biomed. Pharmacother.* **2008**, *62*, 199–207.
- (9) Helal, C. J.; Kang, Z.; Lucas, J. C.; Gant, T.; Ahljanian, M. K.; Schachter, J. B.; Richter, K. E. G.; Cook, J. M.; Menniti, F. S.; Kelly, K.; Mente, S.; Pandit, J.; Hosea, N. Potent and cellularly active 4-aminoimidazole inhibitors of cyclin-dependent kinase 5/p25 for the treatment of Alzheimer's disease. *Bioorg. Med. Chem. Lett.* **2009**, *19*, 5703–5707.
- (10) Rosini, M.; Simoni, E.; Milelli, A.; Minarini, A.; Melchiorre, C. Oxidative Stress in Alzheimer's Disease: Are We Connecting the Dots? *J. Med. Chem.* **2014**, *57*, 2821–2831.
- (11) Li, D.-D.; Zhang, Y.-H.; Zhang, W.; Zhao, P. Meta-Analysis of Randomized Controlled Trials on the Efficacy and Safety of Donepezil, Galantamine, Rivastigmine, and Memantine for the Treatment of Alzheimer's Disease. *Front. Neurosci.* **2019**, *13*, 472.
- (12) Wilkaniec, A.; Gąssowska-Dobrowolska, M.; Strawski, M.; Adamczyk, A.; Czapski, G. A. Inhibition of cyclin-dependent kinase 5 affects early neuroinflammatory signalling in murine model of amyloid beta toxicity. *J. Neuroinflammation* **2018**, *15*, 1.
- (13) Ritchie, C. W.; Ames, D.; Clayton, T.; Lai, R. Metaanalysis of randomized trials of the efficacy and safety of donepezil, galantamine,

and rivastigmine for the treatment of Alzheimer disease. *Am. J. Geriatr. Psychiatr.* **2004**, *12*, 358–369.

(14) Olivares, D.; Deshpande, V. K.; Shi, Y.; Lahiri, D. K.; Greig, N. H.; Rogers, J. T.; Huang, X. N-methyl D-aspartate (NMDA) receptor antagonists and memantine treatment for Alzheimer's disease, vascular dementia and Parkinson's disease. *Curr. Alzheimer Res.* **2012**, *9*, 746–758.

(15) Zheng, Y.-L.; Kesavapany, S.; Gravel, M.; Hamilton, R. S.; Schubert, M.; Amin, N.; Albers, W.; Grant, P.; Pant, H. C. A Cdk5 inhibitory peptide reduces tau hyperphosphorylation and apoptosis in neurons. *EMBO J.* **2005**, *24*, 209–220.

(16) Shukla, V.; Zheng, Y. L.; Mishra, S. K.; Amin, N. D.; Steiner, J.; Grant, P.; Kesavapany, S.; Pant, H. C. A truncated peptide from p35, a Cdk5 activator, prevents Alzheimer's disease phenotypes in model mice. *FASEB J.* **2013**, *27*, 174–186.

(17) Zheng, Y.-L.; Amin, N. D.; Hu, Y.-F.; Rudrabhatla, P.; Shukla, V.; Kanungo, J.; Kesavapany, S.; Grant, P.; Albers, W.; Pant, H. C. A 24-residue peptide (p5), derived from p35, the Cdk5 neuronal activator, specifically inhibits Cdk5-p25 hyperactivity and tau hyperphosphorylation. *J. Biol. Chem.* **2010**, *285*, 34202–34212.

(18) Binukumar, B. K.; Zheng, Y.-L.; Shukla, V.; Amin, N. D.; Grant, P.; Pant, H. C. TFP5, a peptide derived from p35, a Cdk5 neuronal activator, rescues cortical neurons from glucose toxicity. *J. Alzheimer's Dis.* **2014**, *39*, 899–909.

(19) Cardone, A.; Brady, M.; Sriram, R.; Pant, H. C.; Hassan, S. A. Computational study of the inhibitory mechanism of the kinase CDK5 hyperactivity by peptide p5 and derivation of a pharmacophore. *J. Comput.-Aided Mol. Des.* **2016**, *30*, 513–521.

(20) Otyepka, M.; Bártoňová, I.; Kříž, Z.; Koča, J. Different Mechanisms of CDK5 and CDK2 Activation as Revealed by CDK5/p25 and CDK2/Cyclin A Dynamics. *J. Biol. Chem.* **2006**, *281*, 7271–7281.

(21) Tarricone, C.; Dhavan, R.; Peng, J.; Areces, L. B.; Tsai, L.-H.; Musacchio, A. Structure and Regulation of the CDK5-p25nck5a Complex. *Mol. Cell* **2001**, *8*, 657–669.

(22) Mapelli, M.; Musacchio, A. The Structural Perspective on CDK5. *Neurosignals* **2003**, *12*, 164–172.

(23) Rose, P. W.; Prlić, A.; Altunkaya, A.; Bi, C.; Bradley, A. R.; Christie, C. H.; Costanzo, L. D.; Duarte, J. M.; Dutta, S.; Feng, Z.; Green, R. K.; Goodsell, D. S.; Hudson, B.; Kalro, T.; Lowe, R.; Peisach, E.; Randle, C.; Rose, A. S.; Shao, C.; Tao, Y. P.; Valasatava, Y.; Voigt, M.; Westbrook, J. D.; Woo, J.; Yang, H.; Young, J. Y.; Zardecki, C.; Berman, H. M.; Burley, S. K. The RCSB protein data bank: integrative view of protein, gene and 3D structural information. *Nucleic Acids Res.* **2017**, *45*, D271–D281.

(24) Mapelli, M.; Massimiliano, L.; Crovace, C.; Seeliger, M. A.; Tsai, L.-H.; Meijer, L.; Musacchio, A. Mechanism of CDK5/p25 Binding by CDK Inhibitors. *J. Med. Chem.* **2005**, *48*, 671–679.

(25) Binukumar, B. K.; Shukla, V.; Amin, N. D.; Bhaskar, M.; Skuntz, S.; Steiner, J.; Winkler, D.; Pelech, S. L.; Pant, H. C. Analysis of the Inhibitory Elements in the p5 Peptide Fragment of the CDK5 Activator, p35, CDKR1 Protein. *J. Alzheimer's Dis.* **2015**, *48*, 1009–1017.

(26) Steinbach, P. J. Exploring peptide energy landscapes: A test of force fields and implicit solvent models. *Proteins: Struct., Funct., Bioinf.* **2004**, *57*, 665–677.

(27) Brooks, B. R.; Brooks, C. L.; Mackerell, A. D.; Nilsson, L.; Petrella, R. J.; Roux, B.; Won, Y.; Archontis, G.; Bartels, C.; Boresch, S.; Caffisch, A.; Caves, L.; Cui, Q.; Dinner, A. R.; Feig, M.; Fischer, S.; Gao, J.; Hodoscek, M.; Im, W.; Kuczera, K.; Lazaridis, T.; Ma, J.; Ovchinnikov, V.; Paci, E.; Pastor, R. W.; Post, C. B.; Pu, J. Z.; Schaefer, M.; Tidor, B.; Venable, R. M.; Woodcock, H. L.; Wu, X.; Yang, W.; York, D. M.; Karplus, M. CHARMM: The Biomolecular Simulation Program. *J. Comput. Chem.* **2009**, *30*, 1545–1614.

(28) Huang, J.; MacKerell, A. D., Jr. CHARMM36 all-atom additive protein force field: validation based on comparison to NMR data. *J. Comput. Chem.* **2013**, *34*, 2135–2145.

(29) Best, R. B.; Zhu, X.; Shim, J.; Lopes, P. E. M.; Mittal, J.; Feig, M.; MacKerell, A. D. Optimization of the Additive CHARMM All-Atom Protein Force Field Targeting Improved Sampling of the Backbone ϕ, ψ

and Side-Chain χ_1 and χ_2 Dihedral Angles. *J. Chem. Theory Comput.* **2012**, *8*, 3257–3273.

(30) Hassan, S. A.; Mehler, E. L.; Zhang, D.; Weinstein, H. Molecular dynamics simulations of peptides and proteins with a continuum electrostatic model based on screened Coulomb potentials. *Proteins* **2003**, *51*, 109–125.

(31) Hassan, S. A.; Mehler, E. L. From quantum chemistry and the classical theory of polar liquids to continuum approximations in molecular mechanics calculations. *Int. J. Quantum Chem.* **2005**, *102*, 986–1001.

(32) Cardone, A.; Pant, H.; Hassan, S. A. Specific and Non-Specific Protein Association in Solution: Computation of Solvent Effects and Prediction of First-Encounter Modes for Efficient Configurational Bias Monte Carlo Simulations. *J. Phys. Chem. B* **2013**, *117*, 12360–12374.

(33) Jo, S.; Kim, T.; Iyer, V. G.; Im, W. CHARMM-GUI: A web-based graphical user interface for CHARMM. *J. Comput. Chem.* **2008**, *29*, 1859–1865.

(34) Lee, J.; Cheng, X.; Swails, J. M.; Yeom, M. S.; Eastman, P. K.; Lemkul, J. A.; Wei, S.; Buckner, J.; Jeong, J. C.; Qi, Y.; Jo, S.; Pande, V. S.; Case, D. A.; Brooks, C. L.; MacKerell, A. D.; Klauda, J. B.; Im, W. CHARMM-GUI Input Generator for NAMD, GROMACS, AMBER, OpenMM, and CHARMM/OpenMM Simulations Using the CHARMM36 Additive Force Field. *J. Chem. Theory Comput.* **2016**, *12*, 405–413.

(35) Durell, S. R.; Brooks, B. R.; Ben-Naim, A. Solvent-Induced Forces Between Two Hydrophilic Groups. *J. Phys. Chem.* **1994**, *98*, 2198–2202.

(36) Jorgensen, W. L.; Chandrasekhar, J.; Madura, J. D.; Impey, R. W.; Klein, M. L. Comparison of Simple Potential Functions for simulating Liquid Water. *J. Chem. Phys.* **1983**, *79*, 926–935.

(37) Hoover, W. G. Canonical dynamics: Equilibrium phase-space distributions. *Phys. Rev. A* **1985**, *31*, 1695–1697.

(38) Feller, S. E.; Zhang, Y.; Pastor, R. W.; Brooks, B. R. Constant pressure molecular dynamics simulation: The Langevin piston method. *J. Chem. Phys.* **1995**, *103*, 4613–4621.

(39) Ebeling, W.; Gudowska-Nowak, E.; Sokolov, I. M. On Stochastic Dynamics In Physics —Remarks On History And Terminology. *Acta Phys. Pol., B* **2008**, *39*, 1003.

(40) Martyna, G. J.; Tobias, D. J.; Klein, M. L. Constant-Pressure Molecular-Dynamics Algorithms. *J. Chem. Phys.* **1994**, *101*, 4177–4189.

(41) Sagui, C.; Darden, T. A. Molecular dynamics simulations of biomolecules: Long-range electrostatic effects. *Annu. Rev. Biophys. Biomol. Struct.* **1999**, *28*, 155–179.

(42) Steinbach, P. J.; Brooks, B. R. New spherical-cutoff methods for long-range forces in macromolecular simulation. *J. Comput. Chem.* **1994**, *15*, 667–683.

(43) Darden, T.; York, D.; Pedersen, L. Particle mesh Ewald: An $N \log(N)$ method for Ewald sums in large systems. *J. Chem. Phys.* **1993**, *98*, 10089–10092.

(44) Phillips, J. C.; Braun, R.; Wang, W.; Gumbart, J.; Tajkhorshid, E.; Villa, E.; Chipot, C.; Skeel, R. D.; Kalé, L.; Schulten, K. Scalable molecular dynamics with NAMD. *J. Comput. Chem.* **2005**, *26*, 1781–1802.

(45) Grant, B. J.; Rodrigues, A. F.; ElSawy, K. M.; McCammon, J. A.; Caves, L. S. D. Bio3d: an R package for the comparative analysis of protein structures. *Bioinformatics* **2006**, *22*, 2695.

(46) Skjærven, L.; Yao, X.-Q.; Scarabelli, G.; Grant, B. J. Integrating Protein Structural Dynamics and Evolutionary Analysis with Bio3D. *BMC Bioinf.* **2014**, *15*, 399.

(47) Amadei, A.; Linssen, A. B. M.; Berendsen, H. J. C. Essential dynamics of proteins. *Proteins* **1993**, *17*, 412–425.

(48) Ichiye, T.; Karplus, M. Collective motions in proteins: a covariance analysis of atomic fluctuations in molecular dynamics and normal mode simulations. *Proteins* **1991**, *11*, 205–217.